Magnetic structure evolution and magnetoelastic coupling across the spin reorientation transition in $TmCrO_3$

Vishesh Sharma,[1] Gaurav Gautam,[1] Poonam Yadav,[2] Chin-Wei Wang,[3] Kaya Wei,[4] N. P. Lalla,[5] Theo Siegrist,[4,6] and Shivani Sharma[4,*]

[1]*Department of Physics, Graphic Era Hill University, Dehradun 248002, India*
[2]*Independent Researcher, Mumbai, India*
[3]*National Synchrotron Radiation Research Center, Hsinchu 300092, Taiwan*
[4]*National High Magnetic Field Laboratory, Tallahassee, FL 32310, USA*
[5]*UGC-DAE Consortium for Scientific Research, Indore, Madhya Pradesh, India*
[6]*Department of Chemical and Biomedical Engineering, FAMU-FSU College of Engineering, Florida State University, Tallahassee FL 32310, USA*

(Received 12 November 2025; accepted 23 January 2026; published 17 February 2026)

We present a comprehensive study of the magnetic structure evolution, employing bulk magnetization and neutron powder diffraction (NPD) measurements down to 3.5 K, across the spin reorientation transition in orthorhombic (*Pnma*) $TmCrO_3$. Magnetic susceptibility reveals canted antiferromagnetic (CAFM) ordering at $T_N = 125$ K, followed by the magnetization reversal, showing minima between the two compensation points T_{comp1} and T_{comp2}. Heat capacity shows a λ-transition at T_N, associated with long-range antiferromagnetic order of Cr, followed by a broad feature at ∼ 9 K, arising due to Schottky-type anomaly. Magnetic refinement of NPD data establishes the $Pn'm'a$: $\Gamma2(C_x, G_y; C_x^{Tm}, F_z^{Tm})$ CAFM structure below T_N. A gradual change in magnetic structure occurs during the spin-reorientation (SRO) transition below 30 K. During this, the magnetic structure gradually changes from $Pn'm'a$ (Γ2) to $Pn'ma'$ (Γ4): $A_x, F_y, G_z; F_y^{Tm}$. Below 30 K, however, neither Γ2 nor Γ4 alone adequately fit the intensity of magnetic reflections. A satisfactory refinement could only be achieved in the monoclinic subgroup $P2'_1/c'$ derived from a combination of Γ2 and Γ4. The observed gradual SRO of Tm and Cr moments is consistent with the magnetic symmetry $P2'_1/c'$: $C_x, G_y, G_z; C_x^{Tm}, F_y^{Tm}, F_z^{Tm}$. Furthermore, the ordered moments Cr and Tm in $TmCrO_3$ exhibit a complex, nonmonotonic temperature dependence as expected during SRO. Anomalies in lattice parameters suggest magnetoelastic coupling, linking structural distortions to the SRO.

DOI: 10.1103/2bh3-t78c

I. INTRODUCTION

Rare earth (RE) perovskite oxides with transition metal (TM) ion (Fe, Cr, V) at the B-site have been extensively studied for exhibiting complex magnetism, including spin-reorientation (SRO) transition, multiferroicity, spin-phonon coupling, and temperature-induced magnetization reversal [1–5]. Most of these compounds crystallize in a centrosymmetric orthorhombic phase *Pnma* (No. 62, $GdFeO_3$-type) where transition metal (TM) ions occupy the 4b site, forming a distorted TM-O_6 octahedra. With changing temperature, these distortions affect the magnetic response, leading to SRO transition, followed by magnetization reversal [6–8]. In these perovskites, magnetization reversal occurs during field-cooled cooling (FCC) curve below the TM-canted antiferromagnetic (CAFM) ordering temperature T_N. During FCC, the net magnetization of the antiparallel polarized paramagnetic RE moments, against the net sublattice magnetization arising from the uncompensated TM moments of the CAFM order, overcompensates it below T_{comp} [9–12]. Antiparallel polarization of the paramagnetic RE moments results from the negative super-exchange interaction between TM-O-RE. This phenomenon has been widely reported in rare-earth vanadates, ferrites, and chromates, which is supposed to arise from the delicate interplay between the 3d transition-metal and the 4f rare-earth sublattices [4,7,13].

Magnetization reversal is intriguing both for its fundamental importance and for applications in spintronic devices such as magnetic switches and spin-valves, which exploit two stable magnetic states under an external field [14,15]. In systems exhibiting this behavior, the SRO is typically followed by a compensation temperature T_{comp}, at which the sublattice magnetizations cancel each other, yielding zero net magnetization. Upon further cooling below T_{comp}, the imbalance between antiferromagnetically coupled sublattices drives the net magnetization negative, before recovering a positive value at still lower temperatures. This trend of magnetic phenomena is observed for most of the orthochromates and orthoferrites [3,9,16–21]. On the other hand, in nonmagnetic rare-earth vanadate, such as YVO_3, the magnetization reversal originates from the coexistence of competing magnetic phases, which is intimately coupled to the underlying structural phase transition [7]. The phenomenon of magnetization reversal has not only been observed in perovskites but has also been widely observed in different classes of materials such as spinel, alloys, and garnets [22–27].

*Contact author: phy.shivanisharma@gmail.com

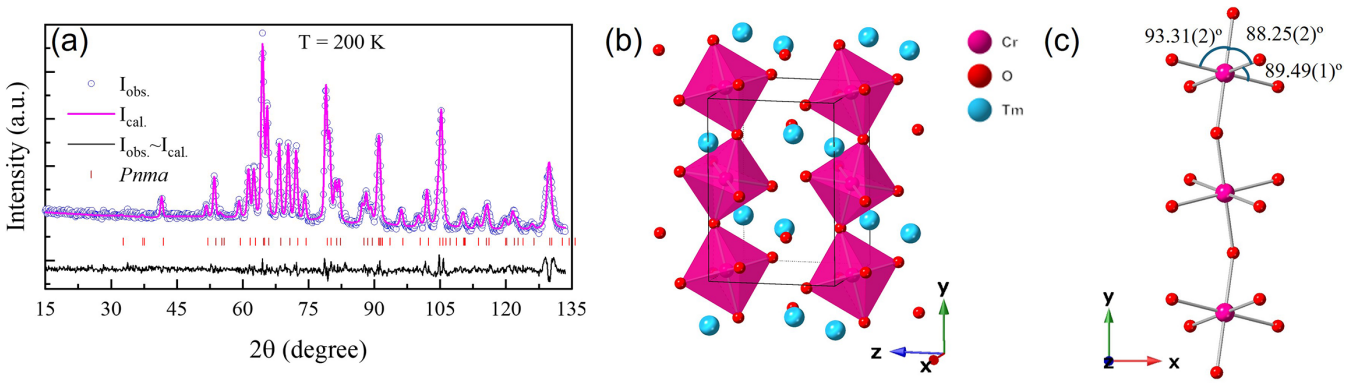

FIG. 1. (a) Rietveld refined 200 K NPD pattern of $TmCrO_3$. (b) Crystal structure of $TmCrO_3$ made based on the refined parameters. This highlights the tilted CrO_6 octahedra (pink) forming a corner-shared network. (c) Octahedral chain along the *c*-axis, highlighting the Cr–O–Cr bond angle and illustrating the distortions in the CrO_6 octahedra.

Bulk magnetization measurements on $TmCrO_3$ (TCO) reveal long-range CAFM ordering at ∼125 K, followed by two successive magnetization reversals: the first near 30 K and a second at lower temperatures around 11 K [9,28]. The first compensation temperature (∼30 K) has previously been attributed to antiparallel coupling between the rare-earth (Tm) and Cr sublattices [29], whereas the origin of the second reversal in isostructural $GdCrO_3$ has recently been attributed to the flipping of net magnetization along the applied field (H) in order to minimize the Zeman energy [12]. In addition, TCO exhibits both magnetocaloric and exchange bias effects [9,28]. Despite all these studies, direct evidence for the evolution of the magnetic structure in TCO is missing from the literature. In this work, we present neutron powder diffraction, magnetization, and heat capacity results that reveal the microscopic origin of these anomalies. Our analysis confirms that TCO undergoes AFM ordering of Cr ions at $T_N = 125$ K with Γ2 spin configuration. Below 50 K, the system enters a spin-reorientation regime involving a transition from the Γ2 to Γ4 configuration. However, instead of stabilizing in a single configuration, TCO retains a mixed Γ2/ Γ4 state even down to 3.5 K, giving rise to a complex magnetic ground state with $P2'_1/c'$ monoclinic symmetry. Anomalies observed in the lattice parameters appear to correlate with the compensation points, suggesting possible magnetoelastic coupling in the system. Neutron-based symmetry analysis, together with detailed magnetic structure evolution, reveals a complex and nonmonotonic temperature dependence of Tm and Cr magnetic moments in TCO below SRO.

II. EXPERIMENTAL

The solid-state reaction method has been used to synthesize polycrystalline $TmCrO_3$ [9]. Elemental composition of thulium (Tm) and chromium (Cr) in a phase-pure sample was determined using energy-dispersive X-ray spectroscopy (EDS) (FEI Quanta). DC magnetization was measured using a Quantum Design SQUID magnetometer under zero-field cooled (ZFC) and field-cooled cooling (FCC) and field-cooled warming (FCW) conditions in an applied field of 0.1 T. The FCC curve was recorded during cooling in an applied magnetic field of 0.1 T, whereas the FCW (or FC) curve was recorded upon warming after cooling the sample in a field of 0.1 T. Heat capacity was measured using a Quantum Design physical property measurement system (PPMS). Powder neutron diffraction measurements on $TmCrO_3$ were carried out at ECHIDNA and WOMBAT beamlines at the OPAL facility, ANSTO, Australia. Data from the WOMBAT beamline with a neutron wavelength of 2.41 Å were used for the magnetic structure analysis in a temperature range from 3.5 K to 120 K. The JANA2006 program suite was used for the magnetic structure refinement [30].

III. RESULTS AND DISCUSSION

Figure 1(a) shows the Rietveld refined 200 K NPD pattern of TCO measured at WOMBAT with $\lambda = 2.41$ Å. This defines the paramagnetic background above the AFM ordering. All structural Bragg peaks are fitted with the *Pnma* structure. Refined values of the structural parameters are given in Table I, and the crystal structure is shown in Fig. 1(b), where the distorted CrO_6 octahedra are shown in pink, Tm atoms in blue, and oxygen atoms in cyan.

Figure 2(a) displays the zero-field cooled (ZFC), field-cooled cooling (FCC), and field-cooled warming (FCW/FC) magnetic susceptibility (χ) of TCO measured with a 0.1 T field. With decreasing temperature, a sharp upturn is observed below 126 K, followed by a peak in the ZFC curve. The transition temperature is determined by the first-order derivative, Fig. 2(b), of ZFC magnetic susceptibility, which gives $T_N = 125$ K, consistent with literature [9,31]. The inset shows the enlarged view around T_N. Below T_N, with decreasing temperature, the FCC susceptibility gradually increases with a broad maxima at ∼ 60 K, below which it leads to crossover with the ZFC and FCW curves. Further below, the magnetization undergoes reversal and turns negative at T_{comp1}, typical to few other orthochromates [9–11]. The sharp upturn in magnetization below minima, leading to T_{comp2}, is attributed to domain-flipping, as a response to minimize the negative Zeman-energy [12]. The sharply rising susceptibility gets saturated at lower temperatures. The FCW and the ZFC curves superimpose each other. The inset in Fig. 2(b) shows the inverse susceptibility ($1/\chi$) of the ZFC curve measured with 1 T. The Curie-Weiss (CW) fit of $1/\chi$ shows linear

TABLE I. Structural parameters of $TmCrO_3$ at 200 K, determined using NPD data. a = 5.4931(4), b = 7.4891(8) and c = 5.2023(5) Å. The values of goodness-of-fitting (GOF) and R_{wp} factor are 2.01 and 5.97, respectively.

Atoms	Wyckoff positions			Occupancies	Uiso (Å^2)
	x	y	z		
Tm	0.0717(8)	0.25	−0.018(1)	1	0.029(2)
Cr	0	0	0.5	1	0.020(2)
O1	0.460(1)	0.25	0.106(1)	1	0.030(2)
O2	0.3030(8)	0.0556(5)	−0.3079(8)	1	0.029(2)

behaviour down to 132 K and yields a value for the Curie constant C = 9.2 corresponding to $\mu_{eff.} = 8.58\,\mu_B$/f.u., close to the expected value of 8.48 μ_B. The Weiss constant of Θ =-33 K indicates AFM interactions, consistent with the M-H isotherms [32].

To further investigate the nature of these magnetic transitions, heat capacity has been measured between 1.8 K and 200 K under zero magnetic field, as shown in Fig. 3. A λ-type transition is observed at 125 K, which is associated with the long-range CAFM order of Cr^{3+}. The heat capacity curve shows another broad feature at ∼ 9 K. This broad feature likely originates from the Schottky anomaly, as seen in $YbCrO_3$ [18]. This is a typical feature seen in various rare-earth-based systems [18,33–35]. Schottky anomaly is usually seen in samples, comprising two-level energy system arising either from the crystal-field effect or due to the presence of an internal field, splitting some degenerate level of Tm^{3+}.

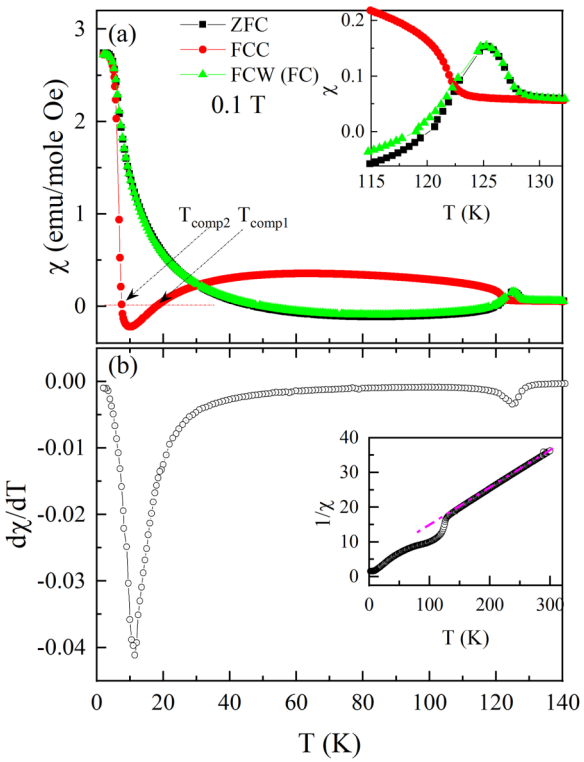

FIG. 2. (a) Temperature-dependent DC magnetic susceptibility (χ_{dc}) of TCO measured at B = 0.1 T field under ZFC, FCC, and FCW conditions. The inset in panel (a) shows the enlarged view around the first transition, highlighted by the red box in the main figure. Arrows indicate the compensation temperatures T_{comp1} and T_{comp2}. (b) First-order derivative of ZFC χ_{dc} (0.1 T) exhibits the first peaks at T_N and between T_{comp1} and T_{comp2}. The inset to panel (b) presents the Curie-Weiss fit of the inverse susceptibility measured under 1 T.

To investigate the magnetic structure as a function of temperature, NPD measurements have been performed at WOMBAT. Figure 4 shows the NPD patterns of TCO measured over a range of temperatures. Below T_N, several additional peaks emerge, with the two most intense magnetic reflections, (110) and (011), appearing near $2\theta = 30^\circ$ as shown in Fig. 4(a). The waterfall NPD plots as a function of temperature are given in Figure S1. Figures 4(b) and 4(c) depict the temperature-dependent peak profiles and integrated intensities of the (110) and (011) peaks below T_N, respectively. The intensities of both peaks increase upon cooling down to 30 K, below which they exhibit distinct temperature dependencies. Below it, the intensity of the (110) reflection increases sharply, while that of the (011) reflection decreases. This divergence suggests a reorientation of the magnetic moments of Tm^{3+} and/or Cr^{3+}, possibly reflecting changes in the relative contributions of the Tm and Cr sublattices to the net magnetic structure. The behavior is linked to the compensation effect, where sublattice magnetizations balance and then reverse dominance as the temperature decreases. In Fig. 4(c), the blue lines serve as a guide to the eye, showing that below 30 K the temperature dependence of (110) and (011) differs markedly.

All the magnetic reflections observed below T_N can be indexed by the propagation vector $k = (0, 0, 0)$. For $k =$

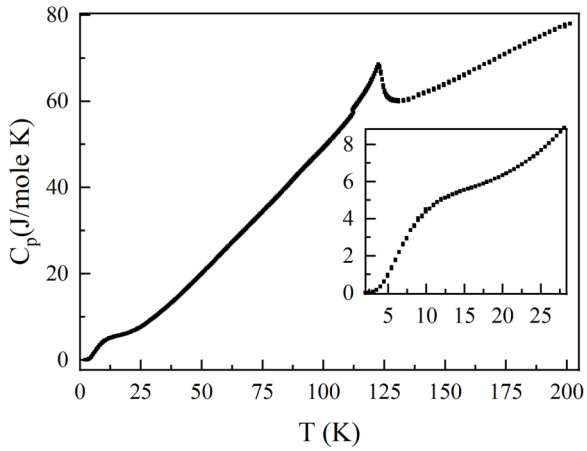

FIG. 3. Temperature-dependent heat capacity of $TmCrO_3$. The inset shows the zoom view for the temperature range of 1.8 to 28 K.

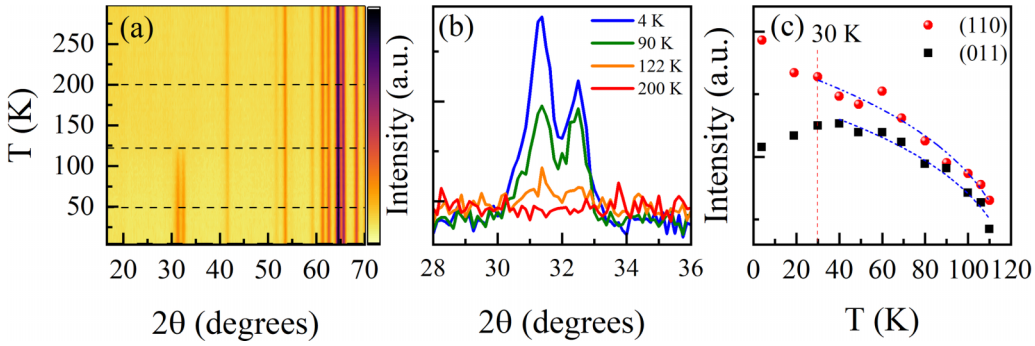

FIG. 4. (a) Thermo-neutron diffractogram of $TmCrO_3$, showing the evolution of magnetic Bragg reflections below T_N. Three horizontal dashed lines in (a) correspond to the temperatures 200, 122, 90, and 4 K shown in (b). (b) Temperature-dependent intensity profiles of the (110) and (011) magnetic reflections. (c) Integrated intensity of the (110) and (011) reflections as a function of temperature. The vertical dashed line marks the boundary below which the peak shows different temperature dependence. Blue dashed lines serve as a guide to the eye.

(0, 0, 0), with Tm and Cr being the magnetic ions, the group analysis results in eight possible maximal magnetic space-groups for the parent space-group *Pnma*. Out of the eight possible magnetic space groups, only four, *Pnma* (Γ1), $Pn'm'a$ (Γ2), $Pnm'a'$ (Γ3), and $Pn'ma'$ (Γ4) yield finite moments at the Cr site. The remaining four models were therefore discarded. The allowed magnetic configurations, Γ1 and Γ3 failed to match the observed intensity of magnetic peaks and can be ruled out. The remaining models, Γ2 and Γ4, were further tested against the data below T_N, and the corresponding fits are shown in Fig. 5. The fit quality of both models was evaluated by examining the most prominent magnetic peaks (110) and (011), [see Figs. 5(a) and 5(b)], which clearly shows improved agreement with the observed data in the case of Γ2, especially down to 25 K. The full patterns at 120 K and 50 K, fitted with Γ2, are given in the Supplemental Material as Fig. S2 [36]. For refining the magnetic structure in Γ2 configuration, the symmetry permits relaxation of all the three magnetic moment components (Ma, Mb, and Mc) for the Cr ions. However, the fitting with all the three components relaxed, which results in nearly negligible values for Ma and Mc. To test this further, we refined the data by constraining Mc = 0, and separately by constraining both Ma and Mc to 0. Setting Mc = 0 does not alter the refinement quality, as the reliability factors remain unchanged compared to that of the unconstrained model. In contrast, fixing both Ma and Mc to zero leads to a slight decrease in the fit quality, indicating a non-zero Ma. For Tm, the Ma and Mc components are symmetry-allowed and were refined under the constraint Ma = −Mc. Following Shamir's notation [37], the magnetic structure in the Γ2 phase can be described as $Pn'm'a$: $\Gamma2(C_x, G_y; C_x^R, F_z^R)$, where the magnetic structure of Cr ions are C-type along x and G-type along y axis whereas the rare-earth Tm moments have C-type ordering along x and F-type along z directions. Similar notations were recently used to define magnetic structures for other members of this family [13,17].

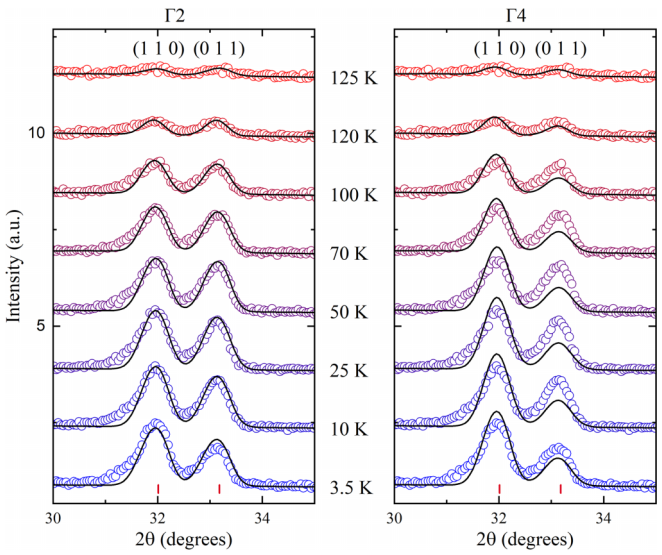

FIG. 5. The zoomed-in view depicting the refinement quality of the most prominent magnetic peaks (110) and (011) using magnetic space groups (a) $Pn'm'a$ (Γ2) and (b) $Pn'ma'$ (Γ4).

For 25 $K < T <$ T_N, the $Pn'm'a$ (Γ2) magnetic model fits the data very well. However, below 25 K, discrepancies begin to appear—specifically, the (110) peak remains underfitted, while the (011) peak gets overfitted. In contrast, the $Pn'ma'$ (Γ4) model provides a poor fit at 25 K and above, though the fitting improves slightly below 25 K. For example, at 3.5 K, with Γ4, the (110) peak is overfitted, and the (011) peak is underfitted, which is opposite to Γ2 model. Thus, neither of the models, while taken individually, provides a satisfactory fit at 3.5 K. A close review of the diffraction data suggests that below 25 K, the transition involves a gradual transformation of $Pn'm'a$ (Γ2) phase to $Pn'ma'$ (Γ4) phase. Therefore, at 10 K and 3.5 K, the system remains in an intermediate state, with spins attaining orientations intermediate to the two magnetic configurations Γ2 and Γ4. Such a spin configuration, suggestive of the coexistence of two phases, at first glance appears to indicate the first-order transition. However, in the absence of any clear anomaly in the heat capacity, this interpretation remains inconclusive.

To fit the data at these temperatures, the magnetic symmetry was reduced to $P2'_1/c'$, a subgroup systematically derived from both $Pn'm'a$ (Γ2) and $Pn'ma'$ (Γ4). This subgroup was

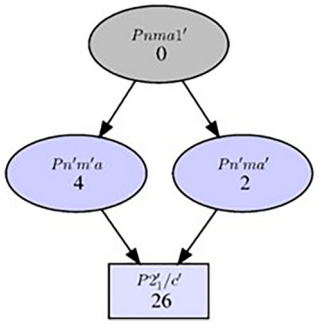

FIG. 6. Diagram illustrating the subgroup lowered from the Γ2 and Γ4 magnetic space groups (MSG), generated using the K-SUBGROUPSMAG tool on the Bilbao Crystallographic Server [38].

identified using the K-SUBGROUPSMAG utility of the Bilbao Crystallographic Server, as given in Fig. 6 [38].

Figures 7(a)–7(c) present comparative fitting of 3.5 K NPD using different models, $Pn'm'a$ (Γ2), $Pn'ma'$ (Γ4), and $P2'_1/c'$. The resulting magnetic structures corresponding to different models are also illustrated in the right panel of Fig. 7. The inset shows an enlarged view of the most prominent magnetic reflections. The possible allowed moment components in different space groups and directions, along with the Tm and Cr coordinates, are listed in Table S1 [36]. Although all three models provide reasonable fits, the $P2'_1/c'$ space group offers the best agreement with the data, as evidenced by its superior fit quality and the lowest R_p and R_{wp} values. Therefore, this model is selected for detailed discussion in the following section. In the monoclinic $P2'_1/c'$ symmetry, the Cr site splits into two positions, which was constrained to have identical moments with opposite signs for all components. All the Mx, My, and Mz components for both Tm and Cr were allowed to be refined. However, refining all of them without the prior knowledge of the magnetic structure above SRO, was a nontrivial task. Therefore, after several iterations, the best quality of fit was achieved. The final magnetic structure below the SRO transition can be best described as $P2'_1/c'$ (C_x, G_y, G_z; C_x^z, F_y^z, F_z^z). The allowed magnetic moment components in different magnetic symmetries are summarized in Table II. For the refined values of magnetic components in different directions in different magnetic space groups, please see Table S2, given in the Supplemental Material [36].

Table III lists the refined magnetic moments of Tm and Cr at selected temperatures. For temperatures between 50 and 100 K, $Pn'm'a$ (Γ2) magnetic space group was used, whereas for temperatures $\leqslant$ 25 K, the $P2'_1/c'$ magnetic space group was employed, as discussed above. The comparative GOF parameters at selected temperatures using $Pn'm'a$ (Γ2), $Pn'ma'$ (Γ4), and $P2'_1/c'$ models are given in Table S3 [36].

TABLE III. Tm and Cr magnetic moments at selected temperatures.

T (K)	Atom	Magnetic moment (M in μ_B)
3.5	Tm	0.81(1)
	Cr	2.02(1)
10	Tm	0.61(14)
	Cr	2.12(15)
25	Tm	0.34(15)
	Cr	2.19(12)
50	Tm	0.27(12)
	Cr	2.11(17)
70	Tm	0.17(16)
	Cr	1.91(13)
100	Tm	0.18(15)
	Cr	1.65(18)

The temperature dependence of the refined ordered moments of Tm (M_{Tm}) and Cr (M_{Cr}) is shown in Fig. 8(a). Upon cooling, the M_{Cr} moment increases rapidly below T_N and saturates to $\sim 2.1\,\mu_B$ at $\sim$ 50 K, and remains nearly constant thereafter. In contrast, M_{Tm} exhibits a nonmonotonic temperature evolution. First, it decreases slightly from $0.25\,\mu_B$ to $0.17\,\mu_B$ near 70 K, then increases again with a sharp enhancement appearing only below 25 K. To highlight the direct correlation with the bulk magnetic response, the ZFC magnetization is overlaid in the background (purple). The anomalous variation of M_{Tm} mirrors the nontrivial behavior of the dc-susceptibility: χ_{dc} initially increases below T_N, peaks near 60 K, and then decreases, eventually dropping below its value above T_N. Furthermore, the sharp rise in M_{Tm} below 30 K coincides with the marked decrease in magnetization, while the additional increase in magnetization below 10 K corresponds to a subtle reduction of M_{Cr} at 3.5 K. This one-to-one correspondence between the evolution of the ordered moments, estimated out of NPD refinment, and the bulk magnetization highlights a complex spin-reorientation process in TCO, where both Cr and Tm moments participate. However, the pronounced temperature dependence of M_{Tm} clearly indicates that the Tm sublattice magnetization plays the dominant role in driving the SRO.

To further explore the structural link of the SRO transition, the temperature evolution of the lattice parameters is presented in Fig. 8(b). The estimated errors in the lattice parameters a, b, and c are of the order of 3E-4 to 4E − 4 Å. All three lattice constants decrease monotonically upon cooling down to $\sim$ 60 K. Below 60 K, the c parameter exhibits an anomalous increase down to ∼30 K, followed by a significant decrease below it. The abrupt increase of the c parameter

TABLE II. Magnetic space group for each magnetic structure models for $TmCrO_3$.

Magnetic space group	Irrep.	Cr			Tm		
$Pn'm'a$	Γ2	C_x	G_y	$F_z\,(=0)$	C_x^{Tm}		F_z^{Tm}
$Pn'ma'$	Γ4	A_x	F_y	G_z		F_y^{Tm}	
$P2'_1/c'$	Γ2+ Γ4	C_x	G_y	G_z	C_x^{Tm}	F_y^{Tm}	F_z^{Tm}

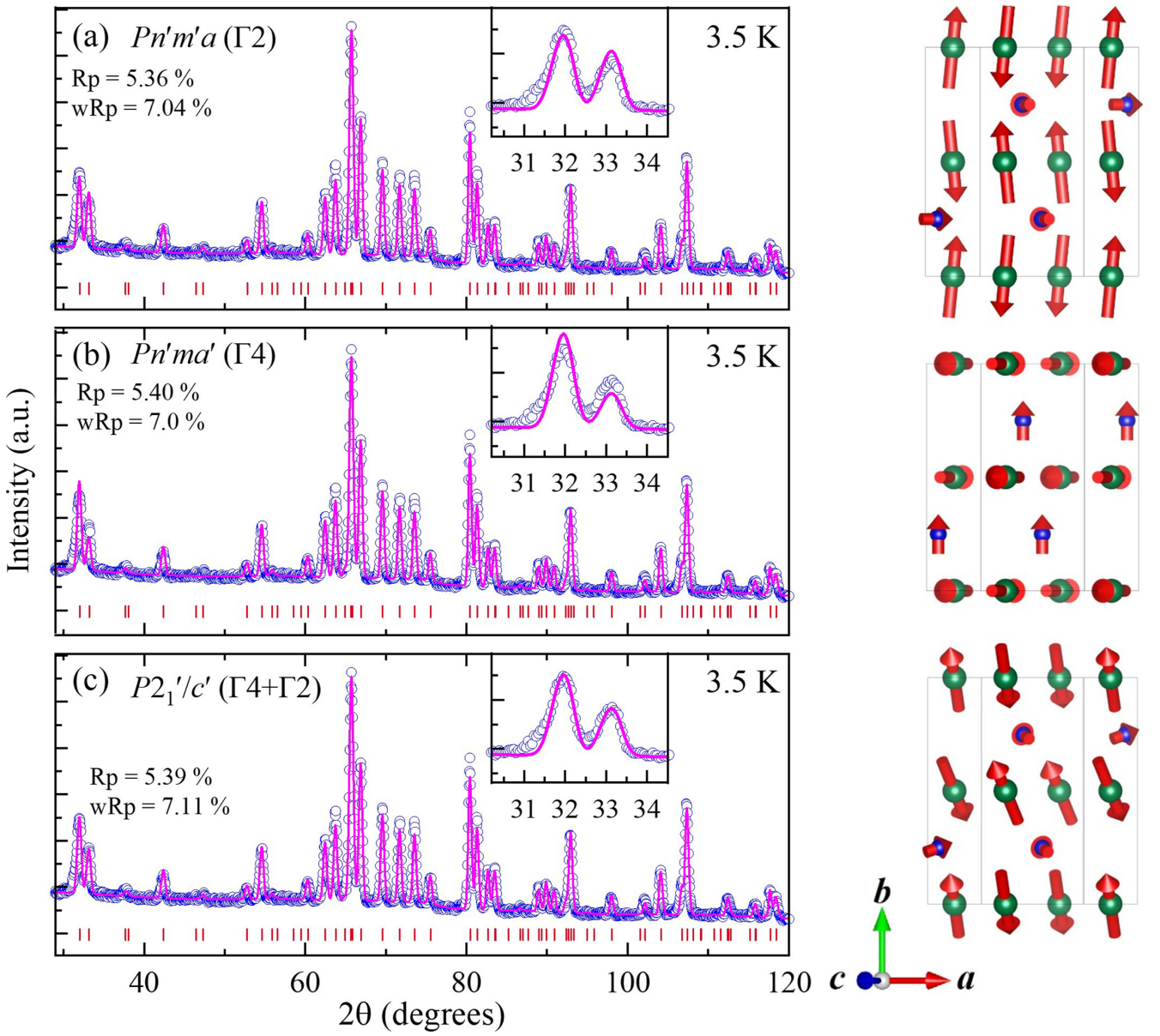

FIG. 7. Comparison of the observed and calculated magnetic diffraction profiles at 3.5 K for the three tested magnetic models: $Pn'm'a$ (Γ2), $Pn'ma'$ (Γ4), and $P2'_1/c'$. Open circles represent the experimental data, while solid lines correspond to the calculated patterns obtained from the Rietveld refinement. Red tick marks indicate the allowed Bragg reflections, and the black line at the bottom shows the difference between the observed and calculated intensities. The reliability factors (Rp and R_{wp}) are indicated for each refinement. The corresponding magnetic structures for Cr (green) and Tm (blue) moments are shown on the right, with arrows indicating the direction of the magnetic moments along the crystallographic axes.

clearly indicates negative thermal expansion for temperatures from 60 to 30 K. In contrast, the *a* and *b* parameters continue to contract across the entire range, albeit with distinct slopes above and below 30 K. Earlier similar nonmonotonic changes in lattice parameters were reported for $YbCrO_3$, which were explained based on temperature variations in Cr-Cr distances via O1 and O2 atoms [18]. It was observed that along O2, the Cr-Cr distance increases, while via O1, it decreases, which led to such nonmonotonic variations in lattice parameters. Similar effects were observed in [39]. In the present case, the lattice parameter *c* increases approximately by 0.02% from 60 to 30 K, which is consistent with the reports on other such systems. The inset of Fig. 8(b) shows the temperature dependence of the lattice volume. While the overall volume decreases continuously with decreasing temperature, the rate of contraction differs across temperature regimes. Above 30 K, the decrease is gradual, whereas below 30 K, it becomes significantly more pronounced. These anomalies in lattice parameters suggest coupling between the lattice and the magnetic response of $TmCrO_3$.

IV. CONCLUSION

In summary, we have investigated the structural and magnetic properties of $TmCrO_3$ using neutron powder diffraction, dc magnetometry, and heat capacity measurements. Magnetic

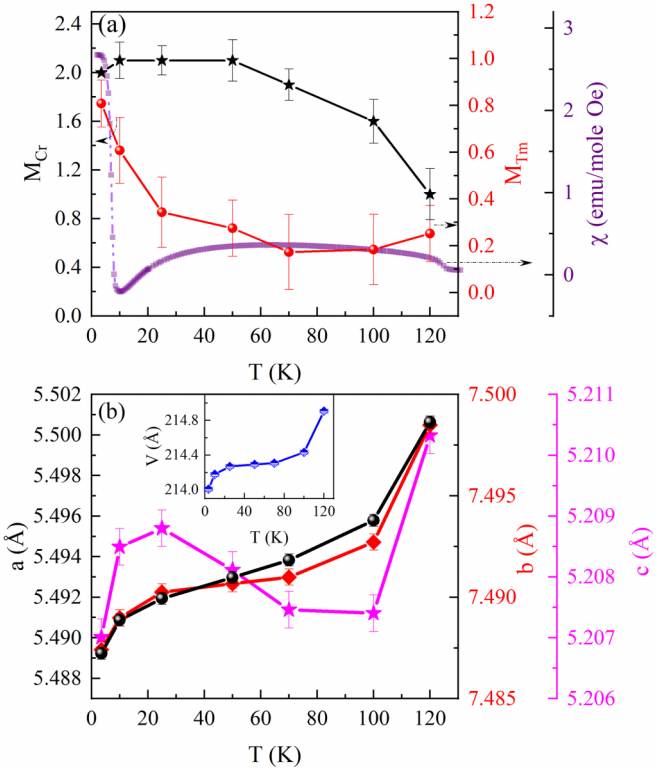

FIG. 8. (a) Temperature dependence of the ordered moments of Cr (black) and Tm (red), plotted together with the ZFC susceptibility (purple, right axis). (b) Temperature evolution of the lattice parameters. The inset to (b) shows the variation in volume expansion as a function of temperature.

susceptibility and heat capacity data reveal long-range antiferromagnetic ordering at $T_N \approx 125$ K, a first compensation point at 18 K, and a second compensation below 8 K, with Curie–Weiss analysis indicating dominant AFM interactions. Below T_N, neutron diffraction identifies the $\Gamma 2$ ($Pn'm'a$) magnetic structure below T_N. Upon further cooling, a complex spin-reorientation transition occurs below 30 K, driven predominantly by the Tm sublattice, which gradually evolves toward the $\Gamma 4$ ($Pn'ma'$) structure. At the lowest temperature 3.5 K, symmetry analysis reveals the change in magnetic symmetry below 30 K. Refinements in the intermediate $P2'_1/c'$ symmetry provide the best description of the magnetic structure, capturing the nonmonotonic change in Cr and Tm moments. The observed anomalies in lattice parameters across the spin-reorientation transition indicate magnetoelastic coupling, suggesting the interplay between structural distortions and magnetic ordering. These results establish $TmCrO_3$ as a prototypical system exhibiting magnetoelastic coupling.

ACKNOWLEDGMENT

A portion of this work was performed at the National High Magnetic Field Laboratory, which is supported by National Science Foundation Cooperative Agreement No. DMR-2128556 and the State of Florida.

DATA AVAILABILITY

The data that support the findings of this article are not publicly available. The data are available from the authors upon reasonable request.

[1] T. Kimura, G. Lawes, T. Goto, Y. Tokura, and A. P. Ramirez, Magnetoelectric phase diagrams of orthorhombic RMnO$_3$ (R = Gd, Tb, and Dy), Phys. Rev. B **71**, 224425 (2005).

[2] T. Kimura, T. Goto, H. Shintani, K. Ishizaka, T. Arima, and Y. Tokura, Magnetic control of ferroelectric polarization, Nature (London) **426**, 55 (2003).

[3] S. Mahana, B. Rakshit, R. Basu, S. Dhara, B. Joseph, U. Manju, S. D. Mahanti, and D. Topwal, Local inversion symmetry breaking and spin-phonon coupling in the perovskite $GdCrO_3$, Phys. Rev. B **96**, 104106 (2017).

[4] T. Yamaguchi and K. Tsushima, Magnetic symmetry of rare-earth orthochromites and orthoferrites, Phys. Rev. B **8**, 5187 (1973).

[5] Y. Tokunaga, S. Iguchi, T. Arima, and Y. Tokura, Magnetic-field-induced ferroelectric state in $DyFeO_3$, Phys. Rev. Lett. **101**, 097205 (2008).

[6] J. Hemberger, S. Lobina, H.-A. Krug von Nidda, N. Tristan, V. Yu. Ivanov, A. A. Mukhin, A. M. Balbashov, and A. Loidl, Complex interplay of $3d$ and $4f$ magnetism in $La_{1-x}Gd_xMnO_3$, Phys. Rev. B **70**, 024414 (2004).

[7] S. Sharma, P. N. Shanbhag, F. Orlandi, P. Manuel, S. Langridge, D. Adroja, M. K. Sanyal, and A. Sundaresan, Symmetry origin of the Dzyaloshinskii–Moriya interaction and magnetization reversal in YVO_3, Inorg. Chem. **60**, 2195 (2021).

[8] A. Kumar and S. M. Yusuf, The phenomenon of negative magnetization and its implications, Phys. Rep. **556**, 1 (2015).

[9] K. Yoshii, Magnetization reversal in $TmCrO_3$, Mater. Res. Bull. **47**, 3243 (2012).

[10] K. Yoshii, Magnetic properties of perovskite $GdCrO_3$, J. Solid State Chem. **159**, 204 (2001).

[11] L. H. Yin, J. Yang, X. C. Kan, W. H. Song, J. M. Dai, and Y. P. Sun, Giant magnetocaloric effect and temperature-induced magnetization jump in $GdCrO_3$ single crystal, J. Appl. Phys. **117**, 133901 (2015).

[12] P. Jain, S. Sharma, R. Baumbach, A. K. Yogi, I. Ishant, M. Majumder, T. Siegrist, M. K. Chattopadhyay, and N. P. Lalla, Structural role in temperature-induced magnetization reversal revealed in distorted perovskite $Gd_{1-x}Y_xCrO_3$, Phys. Rev. B **109**, 094410 (2024).

[13] T. Sau, P. Yadav, S. Sharma, R. Raghunathan, P. Manuel, V. Petricek, U. P. Deshpande, and N. P. Lalla, High-resolution time of flight neutron diffraction and magnetization studies of spin reorientation and polar transitions in $SmCrO_3$, Phys. Rev. B **103**, 144418 (2021).

[14] G. Finocchio, I. N. Krivorotov, L. Torres, R. A. Buhrman, D. C. Ralph, and B. Azzerboni, Magnetization reversal driven by spin-polarized current in exchange-biased nanoscale spin valves, Phys. Rev. B **76**, 174408 (2007).

[15] A. Hirohata, K. Yamada, Y. Nakatani, I.-L. Prejbeanu, B. Diény, P. Pirro, and B. Hillebrands, Review on spintronics: Principles and device applications, J. Magn. Magn. Mater. **509**, 166711 (2020).

[16] T. Sau, S. Sharma, P. Yadav, R. Baumbach, T. Siegrist, A. Banerjee, and N. P. Lalla, First-order nature of the spin-reorientation phase transition in $SmCrO_3$, Phys. Rev. B **106**, 064413 (2022).

[17] S. Yano, C.-W. Wang, Y. Zhu, K. Sun, and H.-F. Li, Magnetic structure and phase transition in a single crystal of $ErCrO_3$, Phys. Rev. B **108**, 174406 (2023).

[18] A. Kumar Deepak and S. M. Yusuf, Intertwined magnetization and exchange bias reversals across compensation temperature in $YbCrO_3$ compound, Phys. Rev. Mater. **5**, 124402 (2021).

[19] R. D. Pierce, R. Wolfe, and L. G. Van Uitert, Spin reorientation in mixed samarium-dysprosium orthoferrites, J. Appl. Phys. **40**, 1241 (1969).

[20] J.-H. Lee, Y. K. Jeong, J. H. Park, M.-A. Oak, H. M. Jang, J. Y. Son, and J. F. Scott, Spin-canting-induced improper ferroelectricity and spontaneous magnetization reversal in $SmFeO_3$, Phys. Rev. Lett. **107**, 117201 (2011).

[21] C.-Y. Kuo, *et al.*, $k = 0$ magnetic structure and absence of ferroelectricity in $SmFeO_3$, Phys. Rev. Lett. **113**, 217203 (2014).

[22] R. Padam, S. Pandya, S. Ravi, A. K. Nigam, S. Ramakrishnan, A. K. Grover, and D. Pal, Magnetic compensation effect and phase reversal of exchange bias field across compensation temperature in multiferroic $Co(Cr_{0.95}Fe_{0.05})_2O_4$, Appl. Phys. Lett. **102**, 112412 (2013).

[23] B. Meng, Q. S. Fu, X. H. Chen, G. S. Gong, C. Chakrabarti, Y. Q. Wang, and S. L. Yuan, Effect of Al substitution on the magnetization reversal and complex magnetic properties of $NiCr_2O_4$ ceramics, Phys. Chem. Chem. Phys. **24**, 4925 (2022).

[24] M. K. Ray, B. Maji, K. Motla, K. P. S., and R. P. Singh, Multiple magnetization reversal and field induced orbital moment switching in intermetallic SmMnSi compound, J. Appl. Phys. **128**, 073909 (2020).

[25] M. Oster, V. Ksenofontov, M. Dürl, and A. Möller, Giant negative magnetization in $Al_{9-x}Fe_xMo_3$, Chem. Mater. **31**, 9317 (2019).

[26] R. Pauthenet, Spontaneous magnetization of some garnet ferrites and the aluminum substituted garnet ferrites, J. Appl. Phys. **29**, 253 (1958).

[27] M. Deb, P. Molho, B. Barbara, and J.-Y. Bigot, Controlling laser-induced magnetization reversal dynamics in a rare-earth iron garnet across the magnetization compensation point, Phys. Rev. B **97**, 134419 (2018).

[28] J. Shi, M. S. Seehra, J. Pfund, S. Yin, and M. Jain, Magnetocaloric properties of $TbCrO_3$ and $TmCrO_3$ and their comparison with those of the other $RCrO_3$ systems (R = Gd, Dy, Ho, and Er), J. Appl. Phys. **134**, 103903 (2023).

[29] R. M. Hornreich, Magnetic interactions and weak ferromagnetism in the rare-earth orthochromites, J. Magn. Magn. Mater. **7**, 280 (1978).

[30] V. Petříček, M. Dušek, and L. Palatinus, Crystallographic computing system JANA2006: General features, Z. Kristallogr. Cryst. Mater. **229**, 345 (2014).

[31] J. A. Hodges, P. Imbert, and A. Schuhl, $TmTO_3$ (T = Al, Fe, Cr and V). A 169Tm Mössbauer study of magnetic and crystal field properties, J. Magn. Magn. Mater. **43**, 101 (1984).

[32] V. Sharma, S. Pokhriyal, D. M. Stojr, A. Sharma, N. P. Lalla, and S. Sharma, Structure, morphology and magnetic properties of $TmCrO_3$, in *AIP Conference Proceedings of 69th DAE Solid State Physics Symposium, Mumbai 2025* (to be published).

[33] S. J. Yuan, Y. M. Cao, L. Li, T. F. Qi, S. X. Cao, J. C. Zhang, L. E. DeLong, and G. Cao, First-order spin reorientation transition and specific-heat anomaly in $CeFeO_3$, J. Appl. Phys. **114**, 113909 (2013).

[34] X. F. Sun, I. Tsukada, T. Suzuki, S. Komiya, and Y. Ando, Large magnetothermal effect and spin-phonon coupling in a parent insulating cuprate $Pr_{1.3}La_{0.7}CuO_4$, Phys. Rev. B **72**, 104501 (2005).

[35] Q. J. Li, Z. Y. Zhao, H. D. Zhou, W. P. Ke, X. M. Wang, C. Fan, X. G. Liu, L. M. Chen, X. Zhao, and X. F. Sun, Paramagnetic ground state with field-induced partial order in $Nd_3Ga_5SiO_{14}$ probed by low-temperature heat transport, Phys. Rev. B **85**, 174438 (2012).

[36] See Supplemental Material at http://link.aps.org/supplemental/10.1103/2bh3-t78c for details.

[37] N. Shamir, H. Shaked, and S. Shtrikman, Magnetic structure of some rare-earth orthochromites, Phys. Rev. B **24**, 6642 (1981).

[38] M. I. Aroyo, J. M. Perez-Mato, C. Capillas, E. Kroumova, S. Ivantchev, G. Madariaga, A. Kirov, and H. Wondratschek, Bilbao Crystallographic Server: I. Databases and crystallographic computing programs,, Z. Kristallogr. Cryst. Mater. **221**, 15 (2006).

[39] F. Pomiro, R. D. Sánchez, G. Cuello, A. Maignan, C. Martin, and R. E. Carbonio, Spin reorientation, magnetization reversal, and negative thermal expansion observed in $RFe_{0.5}Cr_{0.5}O_3$ perovskites (R = Lu, Yb, Tm), Phys. Rev. B **94**, 134402 (2016).